# Dual-Functional Microwire ITO Heater and Sensor Fabricated by Laser Micromachining

Min-Chieh Yu<sup>1,2</sup>, Pin-Chung Huang<sup>1,2</sup>, Wei-Chen Kao<sup>1</sup>, and Ji-Yen Cheng<sup>\*1-4</sup>

<sup>1</sup> Research Center for Applied Sciences, Academia Sinica, Taipei, Taiwan
 <sup>2</sup> Institute of Biophotonics, National Yang Ming Chiao Tung University, Taipei, Taiwan
 <sup>3</sup> Department of Mechanical and Mechatronic Engineering, National Taiwan Ocean University, Keelung, Taiwan
 <sup>4</sup> College of Engineering, Chang Gung University, Taoyuan, Taiwan
 \*Corresponding author's e-mail: jycheng@gate.sinica.edu.tw

This study demonstrates a dual-functional microwire fabricated from Indium Tin Oxide (ITO) film. A nanosecond ultraviolet (UV) laser scriber system is used for the ITO surface scribing. We fabricated two transparent microwire and demonstrated that the single wires achieved both heating and sensing functionalities. For heating purpose, the microwires were applied with a bias voltage for achieving Joule heating effect. The electrical current through the microwire was simultaneously measured for obtaining the resistance of the microwire by Ohm's law. The temperature was thus obtained by the temperature coefficient resistance (TCR) curve of the microwire. We also tested the effect of oxygen plasma treatment on the ITO microwires' TCR. It was found that the TCR slope increased by nearly 20%, indicating enhanced temperature sensitivity. In addition, we analyzed surface morphology and heat-affected zones (HAZ) of the laser-ablated region. The surface characterization showed that longer pulse duration and increased energy density resulted in a significant increase in rim height but not notable surface roughness changes. This dual-functional ITO micrometer heater/sensor enabled a temperature gradient of  $\sim$ 5 °C/ $\mu$ m at 100 °C, which demonstrated its excellent potential for precise thermal control and sensing applications.

DOI: 10.2961/jlmn.2025.03.2015

Keywords: ITO, heater, sensor, laser micromachining, nanosecond UV laser, oxygen plasma, HAZ

# 1. Introduction

Laser micromachining of Indium Tin Oxide (ITO) coated glass is a highly precise and adaptable technique with diverse industrial applications [1, 2]. This process uses a laser to selectively remove or modify the ITO layer on glass substrates, enabling the creation of intricate patterns, fine conductor paths, and microstructures with remarkable precision. ITO is valued for its high electrical conductivity and optical transparency. A thin film can have an optical transmittance of greater than 80%, making it a key material in technologies such as touchscreens, displays, and energy-efficient windows [3]. Laser micromachining provides a flexible, efficient, and cost-effective approach to fabricating complex microdevices, enabling innovations in advanced electronics, optoelectronics, and microfluidics through its versatile material processing capabilities [4].

Due to its excellent thermal responsivity and stability, ITO has been extensively employed in resistive microheaters where uniform and controllable heating is required, such as in lab-on-a-chip systems, microfluidic platforms, and de-icing surfaces [5]. Additionally, its predictable resistance—temperature relationship enables its use as a temperature sensor, particularly in flexible electronics and transparent sensing devices [6]. While the roles of ITO as either a heater or a temperature sensor have been well demonstrated individually, the integration of both functionalities into a single microstructure remains relatively unexplored [7].

In this study, we present dual-functional ITO microwires that simultaneously perform Joule heating and real-time temperature sensing. This dual-function design not only simplifies device architecture but also enables monitoring of temperature gradients at micrometer resolution, allowing for more precise thermal management in microscale systems.

A transparent and clean device is also one of the primary objectives of this study. In the laser patterning of ITO, achieving a balance between complete material removal and substrate preservation is critical. Insufficient laser power often results in incomplete ablation, leaving residual ITO on the surface, whereas excessive power can cause thermal damage or microcracks in the underlying glass substrate. Therefore, precise control of laser parameters is essential to ensure high-quality patterning and maintain device transparency.

Previous studies in our laboratory have demonstrated that the ablation threshold is a key factor in achieving clean and selective ITO removal—an essential requirement for forming well-isolated conduction lines or electrodes [8]. This threshold is typically determined by identifying the minimum laser fluence that produces visible damage to the ITO film, as observed through optical or electron microscopy. By analyzing the size and morphology of ablation spots across a range of fluences, the optimal threshold for minimal yet effective removal can be established [9].

Unlike prior experiments that employed near-infrared (NIR) lasers or visible lasers [8, 10], the present study

utilizes a nanosecond ultraviolet (UV) laser source. UV lasers offer several distinct advantages in ITO processing. They have been widely employed for the patterning of ITO films, as demonstrated in studies that ITO can be patterned on glass by selective laser ablation using UV nanosecond sources and ultrashort (picosecond-femtosecond) pulses; thresholds and feature quality depend strongly on wavelength, pulse width, and scanning overlap [1, 11-16]. Their higher photon energy enhances photochemical interactions, enabling more efficient and localized ablation, while their reduced penetration depth limits thermal diffusion and minimizes damage to the glass substrate. Furthermore, the typically shorter pulse durations of UV lasers reduce heat-affected zones (HAZ) and enhance processing precision [17]. These characteristics make UV laser processing a favorable approach for producing high-resolution, damage-free ITO structures on transparent substrates.

#### 2. Materials and Methods

The ITO-coated slides with two different sheet resistances (5  $\Omega$ /square and 90  $\Omega$ /square, abbreviated as 5  $\Omega$ /sq and 90  $\Omega$ /sq, respectively) were purchased from SCIKET Taiwan (Cat. No. SGAST0001-CUS). The nominal ITO film thicknesses were 350±30 nm, and 26±5 nm, respectively. A commercial grade UV laser scriber system (Marco, Taiwan; Model SMUV3A-S) is used for the ITO surface scribing. The laser wavelength is 355 nm, and the shortest pulse duration is approximately 9 ns, which was measured by a high speed (1 ns rise time) photodiode (Thorlabs, USA; Model DET-210) terminated with a 50  $\Omega$ load. Pulse durations in the range of 14 ns to 35 ns were used in this study. The pulse repetition rate was set at 40 kHz, and the beam scanning speed was 100 mm/sec for scribing patterns on ITO film. The laser output is scanned by the galvanometer mirror scanner (or "galvo scanner" for short) equipped with the laser system and focused using a theta lens with focal length of 200 mm. A scanning area of 175 mm x 175 mm is provided by the system.

Because the pulse duration can vary with changes in laser output power, it is essential to maintain a consistent pulse duration during the engraving process. To achieve this, an optical neutral density (ND) filter is used. By selecting ND filters with different optical densities (OD), the power delivered to the material was adjusted without altering the laser's pulse duration. The optical configuration is illustrated in Fig. 1 (a).

# 2.1 UV laser micromachining

Adopting the methodology from our previously published research, the ITO ablation threshold was determined using two methods. The first method assessed changes in ITO resistance, and the resulting fluence threshold is denoted as ThR. The second method measured the ablated spot size, and the corresponding threshold is referred to as Th $\delta$ .

For determining ThR, a test strip of ITO was prepared, as shown in Fig. 1 (b), using a laser power sufficient to electrically isolate the strip (25 mm in length  $\times$  2.5 mm in width) from the surrounding ITO layer. A single-line laser ablation was then applied to the center of the test strip. The resistance of the strip was measured using a multimeter (Fluke, USA; Model 233). An increase in resistance indicated the removal of the conductive ITO film. Resistances higher than the

maximal reading of the multimeter is denoted as 30 M $\Omega$  in the following results. The ablation threshold was identified as the minimum fluence that produced a measurable increase in the resistance.

Th $\delta$ , was obtained by measuring the ablated spot size under different fluence according to the following equation [9]:

$$\delta^2 = 4\omega_0^2 \left[ \ln \left( E/E_{th} \right) \right], \tag{1}$$

where  $\delta$  is the ablated diameter measured observed under a laser scanning microscope (Keyence, Japan; VK-9700),  $\omega_0$  is the  $1/e^2$  laser focus radius [9, 18], E is the pulse energy causing the corresponding  $\delta$ , and  $E_{th}$  is the threshold pulse energy. The pulse energy is related to the laser power, W, by the following equation:

$$E = W/(fA_{1/e2}),$$
 (2)

where f is the laser pulse repetition rate, and the  $I/e^2$  laser spot area,  $A_{I/e2} = \pi \omega_0^2$ . To determine the laser focus radius  $(\omega_0)$  and the corresponding effective area, values of  $\delta^2$  obtained under varying pulse powers were plotted against the natural logarithm of the pulse energy  $(\ln W)$ . Different pulse powers were achieved by attenuating the laser output using ND filters. A linear relationship was observed in the  $\delta^2$ -ln(W) plot, and the slope of this linear fit was used in subsequent calculations. The threshold pulse energy was identified as the x-intercept of the  $\delta^2$ -ln(W) linear fit and was then used to calculate the threshold fluence. The threshold determined by this method is denoted as Th $\delta$ .

In the spot-size method, based on eq. (1), the slope obtained by the linear fitting of the plot was used to calculate the laser focus radius,  $\omega_0$ . The laser diameter, D, was used to calculate the laser spot area  $A_{1/e2}$ . Then the effective area  $A_{eff}$ , which equals  $(1/2)(A_{1/e2})$ , was derived [19]. The linear fitting was also used to calculate the x-intercept, which corresponds to the power that produced the smallest ablated diameter. The laser fluence at the intercept was divided by  $A_{eff}$  to obtain the threshold,  $\text{Th}\delta$ , for different laser pulse durations and for ITO glass of various sheet resistances.

## 2.2 Design of ITO microwire

As illustrated in Fig. 1 (c), the device integrates two microscale wires (120  $\mu$ m in length  $\times$  5  $\mu$ m in width). Each microwire was used either as a single function sensor wire (S) or a dual function Janus wire (J).

# 2.3 TCR measurement

To enable the application of ITO as a temperature sensor, it is essential to establish an accurate and reproducible temperature coefficient resistance (TCR) calibration curve. In this study, a separate ITO-coated glass substrate with a nominal sheet resistance of  $5\,\Omega/\text{sq}$  was employed as a heater plate ("Heater" in Fig. 1(d)). The heater was connected to a temperature controller (TOHO, Japan; Model TTM-J4) for providing a uniform temperature distribution.

The ITO microwire plate (70 mm in length  $\times$  50 mm in width) was stacked on top of the heater with glass side facing the heater, as shown in Fig. 1 (d).

Electrical connections to the microwires were extended using double-sided conductive copper tape and silver

conductive ink, enabling reliable interfacing with the source meters (Keithley, USA; Model 2400, Model 6430). A constant voltage was applied across the circuit for current measurements and for calculating the corresponding resistance using Ohm's law,  $R = I \times V$ . The temperature of the ITO heater was controlled in the range of 30 °C to 100 °C. Current readings were recorded at 10 °C intervals, and the corresponding resistance values were calculated to construct the TCR curve.

# 2.4 Oxygen plasma treatment

The effect of oxygen plasma treatment on the TCR behavior was investigated. The treatment was applied to the microwire region, using an activation power of 18 W for 100 s under an oxygen pressure of 600 mTorr (Nordson, USA; Model AP-600). Following the plasma treatment, the temperature-dependent electrical measurements were repeated using the same procedure described above, and the resulting TCR curve was plotted to evaluate the impact of surface modification on the microwires' thermal-electrical response.

#### 2.5 Surface analysis

Ablation quality was preliminarily observed by a bright-field microscope (Olympus, Japan; Model BXFM). The ablated spot diameter, surface roughness, and the raised rim along the edges of the laser-scribed ITO patterns were characterized using a laser scanning confocal microscope (Keyence, Japan; Model VK9700). The values of roughness, rim height and rim width were obtained by averaging over 16 µm along the laser ablation line. The extent of ITO layer removal was evaluated via energy-dispersive X-ray spectroscopy (EDS; Oxford Instruments, UK; Model X-MAX150). The signal intensity of indium (In) was used as an indicator to confirm the presence or absence of the ITO thin film on the glass substrate.

Additionally, EDS analysis was employed to investigate changes in the elemental distribution within the microwire region before and after oxygen plasma treatment.

## 2.6 COMSOL simulation of temperature gradient

To verify the temperature gradient measured between the Janus wire and the sensor wire, a finite element simulation was performed using COMSOL Multiphysics.

A three-dimensional heat transfer model (*Heat Transfer in Solids and Fluids* physics interface) was constructed to simulate the temperature gradient induced by a microwire functioning as a heater. In the model, a heating area (120  $\mu m$  in length  $\times$  5  $\mu m$  in width) was placed at the center of a silica glass substrate with dimensions of 15 mm  $\times$  15 mm and a thickness of 0.7 mm. The large substrate area corresponds to the unheated region in our chip design.

For boundary condition settings, the heating area was modeled as a constant heat source with temperature maintained at 393.15 K. In addition, the surrounding substrate was defined with material properties corresponding to silica glass, with thermal conductivity, specific heat capacity, and density taken from standard COMSOL material libraries (thermal conductivity =  $1.38 \text{ W/(m\cdot K)}$ , specific heat capacity =  $703 \text{ J/(kg\cdot K)}$ , density =  $2203 \text{ kg/m}^3$ ).

All external surfaces were applied *Convective Heat Flux* boundary condition using the *External Natural Convection* heat transfer coefficient with the ambient air temperature set to 293.15 K. Surface orientations were specified as vertical for side walls, upward-facing horizontal for the top face, and downward-facing horizontal for the bottom face. Mesh refinement was applied near the heater to accurately capture the temperature gradient.

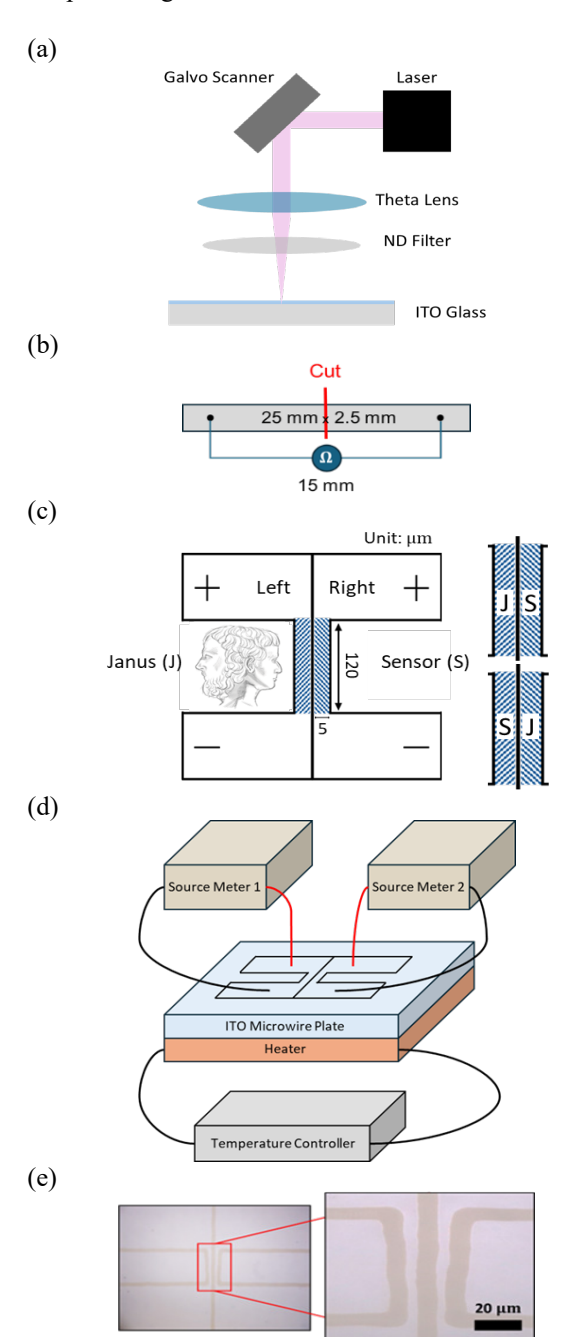


**Fig. 1** (a) The schematic of the laser scribing system. (b) The pattern of the ITO test strip used for measuring the ablation threshold by resistance changes (ThR). The red line indicates the test stroke. (c) The naming rationale and schematic of the Janus dual-function chip. (d) Schematic diagram of the experimental setup for TCR curve measurement. (e) Overview (left-panel) and closed-up (right panel) photo pictures showing the two transparent microwires.

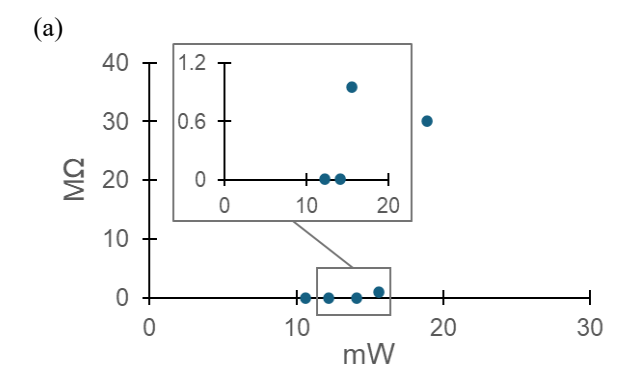
#### 3. Results and Discussion

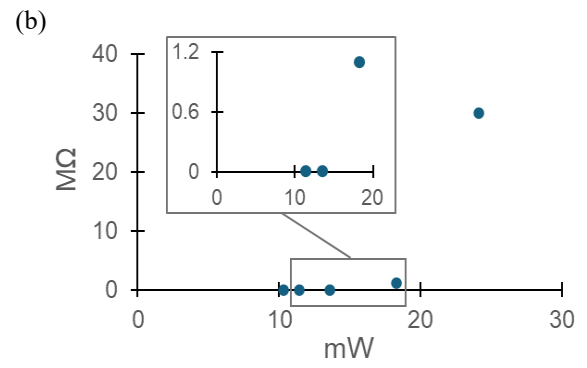
As shown in Fig. 1 (e), the UV laser ablated region is free of microcracks at the underlying glass substrate, indicating the good quality of the ITO pattering by UV laser. Detailed investigation on the ablation parameters is described below.

#### 3.1 Ablation thresholds

To fabricate a transparent and clean chip, we measured the laser ablation thresholds, ThR, and Th $\delta$ , using the two different approaches.

Fig. 2 shows the resistance changes of the ITO test strips after the test stroke ablation under three different conditions. The 30 M $\Omega$  points represent measurements that displayed as OL (overload) on the multimeter. The smallest fluence that resulted in an increase in the test strip resistance was considered as the threshold fluence (ThR).





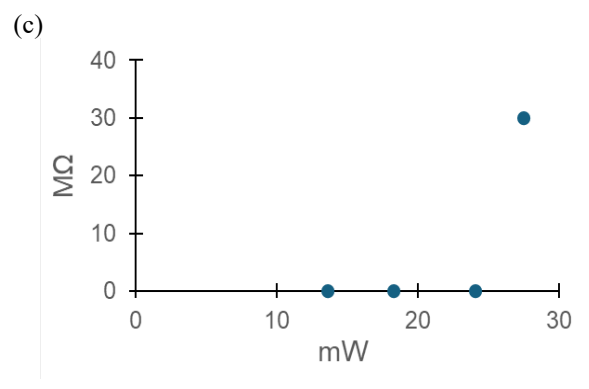


**Fig. 2** The resistance changes of the ITO test strip after the test stroke ablation using different laser powers. (a) 5  $\Omega$ /sq. at 35 ns (b) 5  $\Omega$ /sq. at 14 ns (c) 90  $\Omega$ /sq. at 14 ns. The beam scanning speed was 100 mm/sec.

The second method used the ablated diameter for determining the threshold,  $Th\delta$ , and the laser focus spot diameter (D). Fig. 3 shows the plot of  $\delta^2$  at different laser power, W, on the ITO slides. Based on eq. (1), the slope obtained by the linear fitting of the plot was used to calculate the laser focus radius,  $\omega_0$ . The focus radius and ablation threshold values of the two methods are summarized in Table 1. It is found that smaller threshold is observed by shorter laser pulse on thinner ITO film (i.e. the one with 90  $\Omega$ /sq). The trend is the same for both  $Th\delta$  and ThR. The result is consistent with the fact that shorter laser pulses provide higher transient power and hence the lower threshold.

In addition, thinner ITO film requires lower energy for the ablation. The difference in the apparent focus radius observed for the same laser system was attributed to the Gaussian beam profile. Within a Gaussian beam, thinner ITO films, which has higher sheet resistance, requires less ablation energy and hence is ablated with lower energy density. This resulted in the larger effective ablation area and the larger apparent radius.

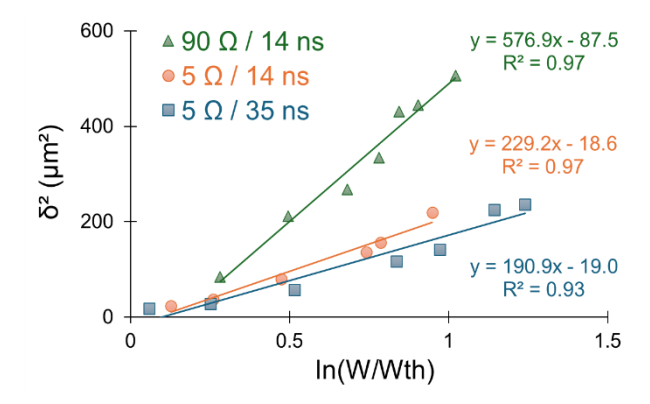


**Fig. 3** The plot of the squared ablated diameter,  $\delta^2$ , as a function of laser power for different parameters. The beam scanning speed was set at 100 mm/s. The insets show the equation and regression coefficient,  $R^2$ , of the linear fitting lines.

**Table 1** The focus radius and ablation thresholds for various ITO sheet resistances and pulse durations. The data includes the following combinations.

Sheet Resistance / Pulse Duration	Focus Radius	ThR (J/cm <sup>2</sup> )	$\frac{Th\delta}{(J/cm^2)}$	
$50 \Omega / 35 ns$	7	0.52	0.50	
50 Ω / 14 ns	8	0.48	0.44	
90 Ω / 14 ns	12	0.30	0.28	

# 3.2 Surface roughness and heat-affected zone

The HAZ refers to the region surrounding the ablated area where laser-induced heat accumulation affects the morphology of the thin film, particularly near the rim. To evaluate the impact of pulse duration and film resistance on laser ablation heat, we measured the surface roughness ( $R_a$ ), rim height ( $Rim_h$ ), and rim width ( $Rim_w$ ) of ITO films processed under different conditions, as shown in Fig. 4 (a).

Typical HAZ of the laser-ablation on the ITO film with 5  $\Omega$ /sq sheet resistance are shown in Fig. 4 (a-b). As shown

in Fig. 4 (c), longer pulses (35 ns) and ITO film with lower sheet resistance (5  $\Omega$ /sq) resulted in a significant increase in rim height with increasing energy density, suggesting stronger heat accumulation and more significant HAZ formation. For the 90  $\Omega$ /sq ITO film, the rim height and rim width are both not significant.

These results are consistent with previous work by Mustafa et al., which showed that extended pulse durations can lead to deeper ablation and more significant thermal effects due to increased energy deposition [20]. Similarly, Kerse et al. demonstrated that increased pulse durations enhance thermal diffusion and amplify the HAZ during ultrafast laser ablation [17].

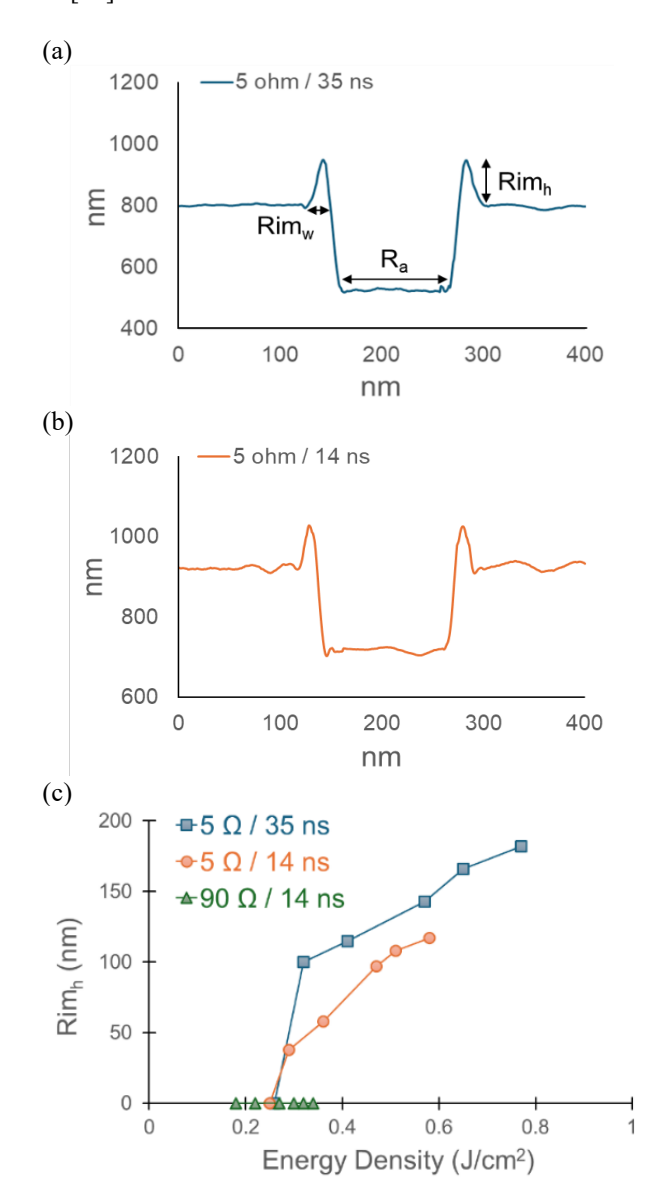


**Fig. 4** The cross-sectional profile of the laser ablated regions observed by the VK laser scanning profiler. (a)  $5 \Omega/\text{sq}$ , 35 ns (b)  $5 \Omega/\text{sq}$ , 14 ns, at an energy density close to  $0.6 \text{ J/cm}^2$ . (a) and (b) have the same scale. (c) Rim height, Rim<sub>h</sub>, as a function of laser energy density under different ablation conditions.

In Table 2, no consistent trend was observed for rim width across different conditions. The average Ra for the three conditions 5  $\Omega$ /sq-35 ns, 5  $\Omega$ /sq-14 ns, and 90  $\Omega$ /sq-14 ns are 91 nm, 72nm, and 66 nm, respectively. It can be seen that the roughness remained similar across different film thicknesses (5  $\Omega$ /sq-14 ns vs. 90  $\Omega$ /sq-14 ns), while it increased with longer pulse duration (5  $\Omega$ /sq-35 ns vs. 5  $\Omega$ /sq-14 ns). This is in accordance with the fact that the glass substrate has little absorption of the UV laser pulse used. In addition, the more significant thermal effects due to increased energy deposition was manifested by the increased surface roughness.

Compared to our previously reported fabrication method utilizing a 1064 nm infrared laser, the UV laser significantly reduced the HAZ and thermal damage to the substrate. Unlike the 1064 nm laser, UV laser processing at a sheet resistance of 90  $\Omega/\text{sq}$  significantly suppresses the formation of raised rim along the edges [8]. The results demonstrated the better ablation surface by the UV laser compared to a 1064 nm NIR laser.

**Table 2** Surface roughness, R<sub>a</sub>, and rim width, Rim<sub>w</sub>, under different ablation conditions, showing no clear dependence on pulse duration or film thickness.

5 Ω / 35 ns		5 Ω / 14 ns			90 Ω / 14 ns			
ED (J/cm <sup>2</sup> )	R <sub>a</sub> (nm)	Rim <sub>w</sub> (nm)	ED (J/cm <sup>2</sup> )	R <sub>a</sub> (nm)	Rim <sub>w</sub> (nm)	ED (J/cm <sup>2</sup> )	R <sub>a</sub> (nm)	Rim <sub>w</sub> (nm)
0.26	92	Х	0.25	70	Х	0.18	67	х
0.32	87	252	0.29	84	201	0.22	55	X
0.41	118	277	0.36	50	239	0.27	61	X
0.57	109	226	0.47	61	251	0.30	78	х
0.65	75	264	0.51	77	222	0.32	69	х
0.77	64	281	0.58	88	242	0.34	64	х

# 3.3 Temperature coefficient of resistance

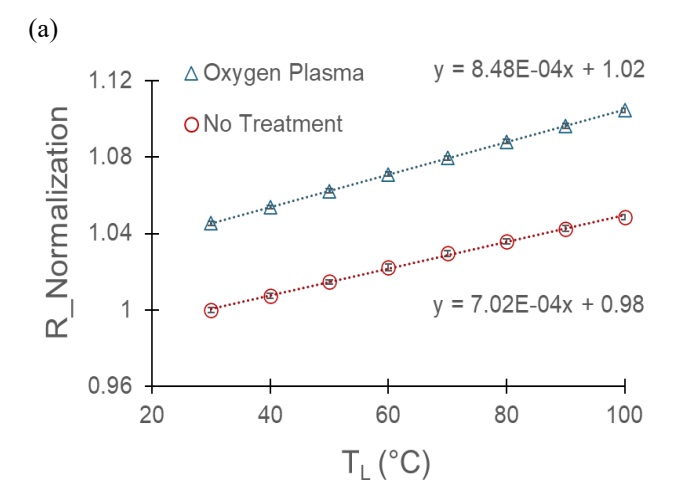
To facilitate subsequent dual-functional microwire experiments, we measured TCR curve of the two ITO microwires. The electrical conductivity of ITO, a degenerate n-type semiconductor, is known to depend on both carrier concentration and mobility—both of which are influenced by temperature and the presence of oxygen vacancies [21].

In our experiment, the microwires' temperatures increased from 30 °C to 100 °C at 10 °C increments. At each step, resistance was determined based on the measured current under a fixed applied voltage (0.5 V). As shown in Fig. 5, the resulting resistance–temperature curve exhibited a positive slope, indicating that resistance increases with temperature. This behavior is characteristic of thermally activated phonon scattering in ITO. As temperature rises, lattice vibrations become more obvious, leading to increased electron–phonon interactions. These interactions reduce carrier mobility, leading to an increase in the material's resistivity. A phenomenon consistent with the Bloch–Grüneisen model for electron–phonon scattering in degenerate semiconductors [22-24].

Following oxygen plasma treatment, the same measurements of TCR were repeated. The treated wire exhibited a 4% higher resistance at 30 °C compared to the untreated wire. Additionally, the TCR slope increased by nearly 20%,

indicating enhanced temperature sensitivity. This change is attributed to a reduction in oxygen vacancies and carrier concentration caused by the oxygen plasma, which is in accordance with a previous work by Lee et al., who demonstrated that oxygen plasma treatment reduces carrier concentration and increases resistivity in ITO films due to the suppression of oxygen vacancies [25].

The result in Fig. 5 were obtained from three repeated measurements, with the microwires' temperature raised from room temperature (RT) to 100 °C, cooled to RT, and then raised again to 100 °C. The entire process lasted for ~ 1 hour. It can be seen that repeated heating/cooling did not result in observable resistance fluctuation, as revealed by the negligible error bars. This result indicates that the microwires showed at least short-term stability. The long-term stability of the microwires requires further verification, as it has been shown that the durability and stability of ITO could change over time under various environmental conditions [26-28].



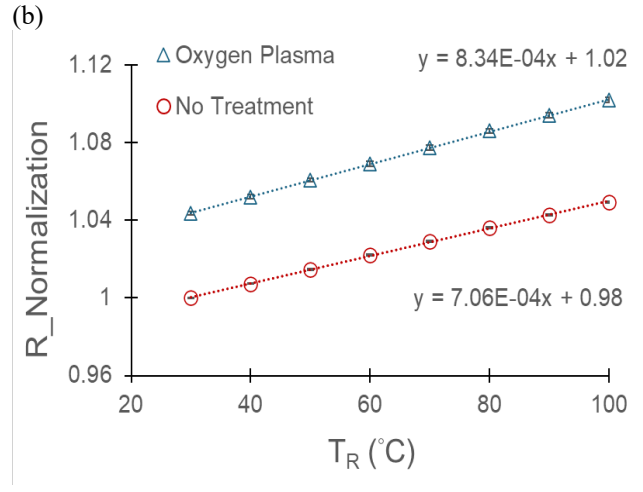


Fig. 5 Curves of the (a) left wire (b) right wire TCR before and after oxygen plasma treatment. The results show a significant increase in resistance and TCR slope after the treatment.

## 3.4 Dual function test

After establishing the TCR curves, we proceeded to evaluate the dual functionality of ITO microwires as both heaters and temperature sensors. In this experiment, one microwire was configured as a Janus wire, simultaneously serving as both heater and sensor, while another microwire functioned solely as a temperature sensor wire.

A voltage ranging from 1 V to 5 V ( $V_J$ ) was applied to the Janus wire for implementing Joule heating. The resulting current was measured using a source meter, and the corresponding resistance was calculated. This resistance was then mapped onto the previously established TCR curve (Fig. 5) to determine the real-time temperature, which was found to increase from approximately 30 °C to 100 °C as the applied voltage increased. The Janus wire is thus acting as a heater and a sensor at the same time.

Simultaneously, the sensor wire was biased with a series of low voltages (0.1 V, 0.2 V, 0.5 V, and 1.0 V) to ensure minimal Joule heating during the measurement. Its resistance, and consequently its temperature, was determined using the same TCR calibration.

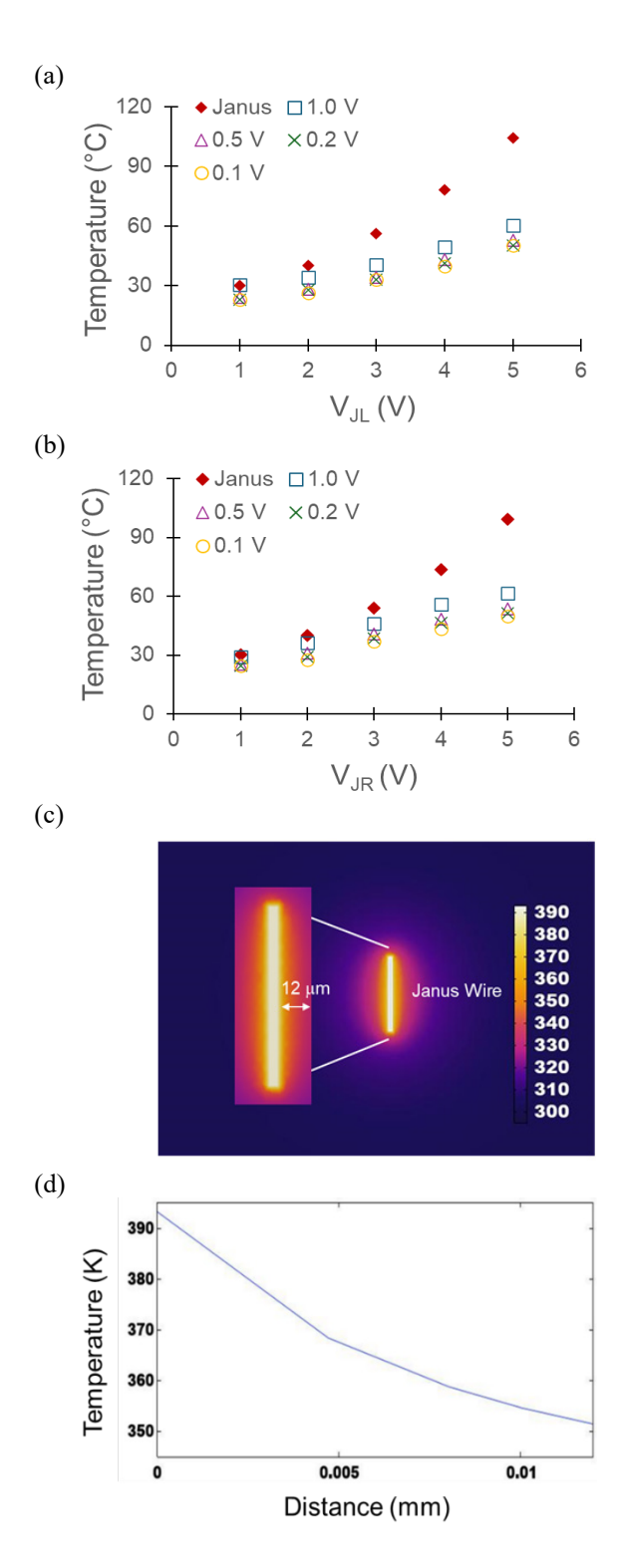
As shown in Fig. 6 (a-b), the Janus wire consistently exhibited higher temperatures than the sensor wire. Based on this temperature difference and the distance between two wires, a thermal gradient of approximately 5 °C/μm was calculated, with the temperature of Janus wire at around 100 °C. This result closely matches the COMSOL simulation result of around 4 °C/μm. In the simulation, the temperature of the Janus wire was set to 100 °C to replicate the experimental conditions. This temperature was selected as it provided the largest temperature difference between the Janus wire and the sensor wire. The simulated temperature distribution and gradient around the Janus wire were illustrated in Fig. 6 (c-d).

It is also seen in Fig. 6 (a-b) that the different voltages of the sensing wire reveal different temperatures. The underlying reason is further investigated as follows.

# 3.5 Self-heating effect of the sensor wire

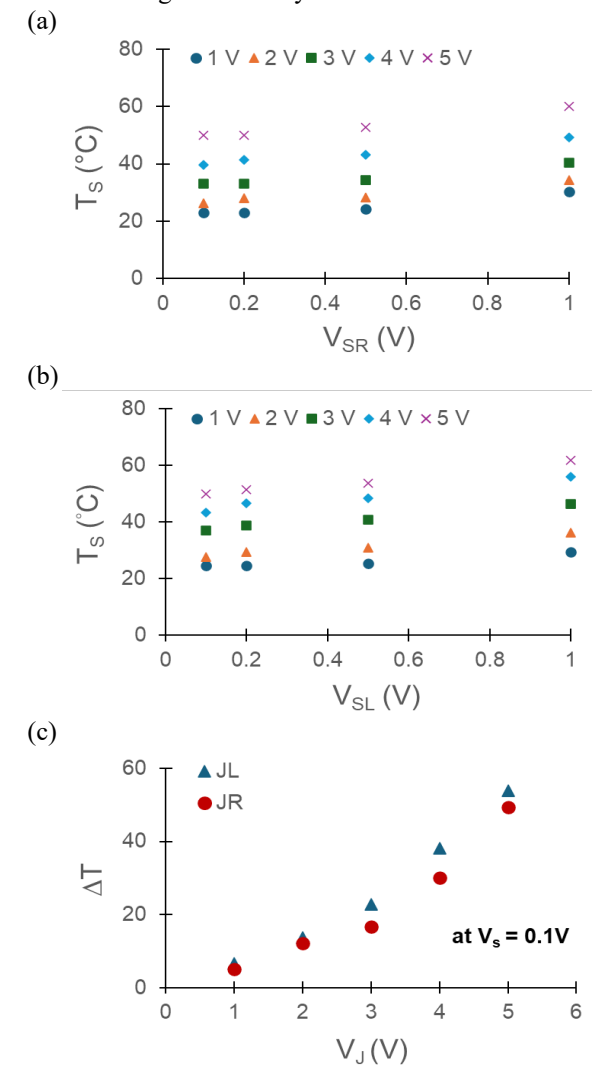
To ensure minimal Joule heating of the sensor wire during the measurement, the effect of sensor wire voltage, V<sub>S</sub>, was investigated. Fig. 7 (a-b) shows that the sensor wire temperature increases with increasing V<sub>S</sub>, indicating heating by the sensor wire during the measurement. The result indicates the necessity to minimize the voltage for obtaining a perturbation-free measurement. With the limited accuracy of the source meter used in this study, the  $V_S = 0.1 \text{ V}$  was used for the following studies and was not reduced further. When the left and right wires are used as Janus wires and the sensor voltage is set at 0.1 V, different temperatures were observed by the Janus wire and the sensor wire, as shown in Fig. 7 (c). This indicates that temperature gradient between the two microwires, Janus and the sensor, did occur. With  $V_J = 5 \text{ V}$ , the temperature difference between the two microwire reaches ~60 °C, resulting in the gradient of ~5 °C/ $\mu$ m, similar to that by the simulation in Fig. 6 (c-d).

Fig. 7 (c) also showed the temperature difference is slightly higher when the left wire was used as the Janus wire. We speculate that this is caused by the difference in the resistances of the two microwire, which led to difference in Joule heating power and the resultant temperature.



**Fig. 6** Temperature of Janus wire and sensor wire with sensor voltage (V<sub>S</sub>) ranged from 0.1 V to 1 V. Voltage for Janus wire (V<sub>J</sub>) of 1 V to 5 V was applied to generate heat while the sensor wire measures the temperature simultaneously. (a) Left microwire as the Janus wire (JL), and (b) Right microwire as the Janus wire (JR). (c) Topview temperature distribution simulated by COMSOL of a single Janus microwire on a glass substrate. The wire temperature was set to 100°C in the simulation. The marked 12 μm indicates the region for the temperature

gradient shown in (d). (d) Simulated temperature gradient extending horizontally from the Janus wire.



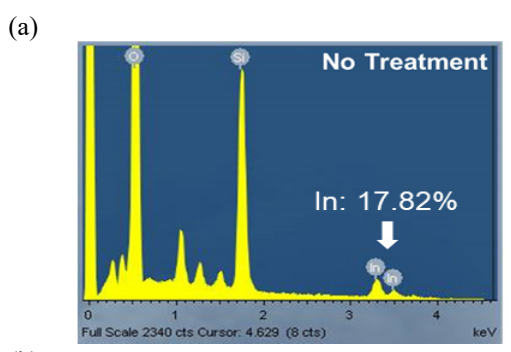
**Fig. 7** Temperature measured by the sensor microwire using different  $V_S$ . (a) Left microwire as the Janus wire (JL) and right wire as the sensor.  $V_{SR}$ : voltage of sensor. (b) Right microwire as the Janus wire (JR) and left wire as the sensor.  $V_{SL}$ : voltage of sensor. (c) Temperature differences are slightly larger with left wire as the Janus wire, as indicated by the blue dots.

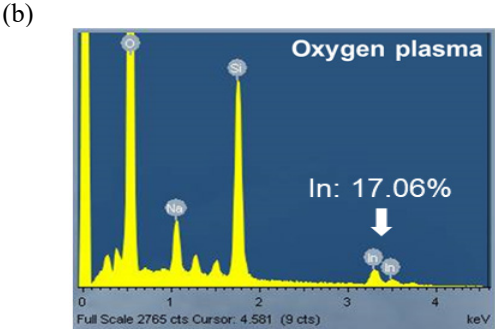
## 3.6 Structure analysis of ITO substrates

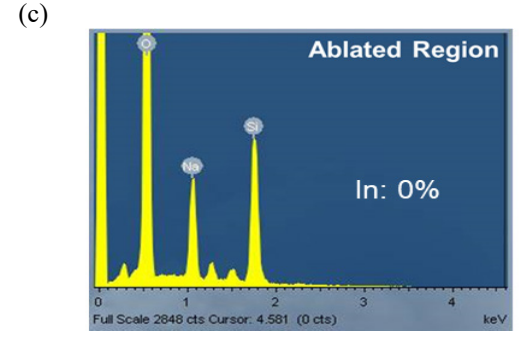
The removal of the ITO layer by the laser ablation was examined using EDS. We measured the distribution of Indium (In) at the laser ablated region and used it as an indicator of the conducting layer.

To further investigate the effect of oxygen plasma treatment, EDS analysis was also performed on the treated ITO chips. However, the elemental mapping showed no significant change in the distribution of indium, tin, or oxygen compared to untreated samples, as shown in Fig. 8 (a-c). This result can be attributed to the intrinsic surface sensitivity and spatial resolution limitations of EDS, which primarily detects compositional differences on the micrometer scale [29]. In contrast, oxygen plasma treatment modified near-surface chemistry primarily within a few nanometers, often through the reduction of oxygen vacancies or slight

changes in bonding states rather than bulk compositional changes detectable by EDS. Similar findings have been reported in previous studies. For example, Park et al. demonstrated that oxygen plasma treatment of ITO films leads to a reduction in oxygen vacancies and free carrier concentration, as evidenced by changes in electrical and optical properties, rather than detectable shifts in elemental concentration via EDS mapping [30]. The reduction of free carrier observed is in consistent with the observed increase of resistance after the plasma treatment (Fig. 5).







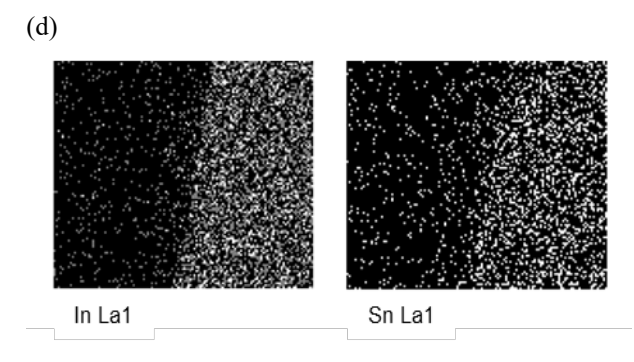


**Fig. 8** EDS spectrum of the ITO microwire region (a) before oxygen plasma treatment, (b) after oxygen plasma treatment, and (c) inside the laser-ablated region. (d) Elemental mapping of indium (In) and tin (Sn).

While O<sub>2</sub> plasma treatment can significantly modify surface properties (e.g., TCR), it may not induce a detectable change in elemental composition within the detection limits of EDS analysis. These results also suggest that the Oxygen plasma effect on TCR may be more prominent on a thin ITO film, such as that with high sheet resistance.

Fig. 8 (d) shows the mapping reveals a clear contrast of indium (In) and tin (Sn) distribution between the laser-ablated and unablated areas. The ablated region shows a sparse Indium signal, indicating effective material removal, while the unetched region retains a dense and uniform distribution, confirming selective laser patterning.

#### 4. Conclusion

In this study, we successfully fabricated a dual-function microscale device using a nanosecond UV laser. Compared to the 1064 nm laser, UV laser processing minimizes thermal damage and HAZ formation while still achieving effective ITO removal, as confirmed by EDS analysis. This advancement marks a notable improvement in the production of transparent electronic devices.

Janus wire represented a single ITO microwire that simultaneously serves as both a Joule heater and a temperature sensor. This dual functionality is unique compared to conventional designs, which typically rely on separate components for heating and sensing. By consolidating both functions into a single element, Janus configuration simplifies system architecture, reduces spatial and wiring complexity, and enhances the feasibility of integration in miniaturized or optically transparent platforms.

Furthermore, by performing simultaneous measurements on two microwires, we successfully monitored the resulting microscale temperature differences, generating a local temperature gradient. This demonstrates the device's ability to spatially resolve thermal distributions with high precision. In summary, this dual-functional ITO micrometer heater/sensor highlights excellent potential for precise thermal control and sensing applications.

# Acknowledgments and Appendixes

The authors thank the partial financial support from National Science and Technology Council, Taiwan. (NSTC 113-2113-M-001-035).

# References

- [1] M.Y. Xu, J. Li, L.D. Lilge, and P.R. Herman: Appl. Phys A, 85, (2006) 7.
- [2] M.F. Chen, W.T. Hsiao, Y.S. Ho, S.F. Tseng, and Y.P. Chen: Thin Solid Films, 518, (2009) 1072.
- [3] C.G. Granqvist: Sol. Energy Mater. Sol. Cells, 91, (2007) 1529.
- [4] A. Nisar, N. AftuIpurkar, B. Mahaisavariya, and A. Tuantranont: Sens. Actuators B Chem., 130, (2008) 917.
- [5] S.K. Jha, R. Chand, D. Han, Y.C. Jang, G.S. Ra, J.S. Kim, B.H. Nahm, and Y.S. Kim: Lab Chip, 12, (2012) 4455.
- [6] H.F. Arata, F. Gillot, T. Nojima, T. Fujii, and H. Fujita: Lab Chip, 8, (2008) 1436.
- [7] N. Lovecchio, V. Di Meo, D. Caputo, A. Nascetti, A. Crescitelli, and E. Esposito: IEEE Sens. J., 21, (2021) 18847.

- [8] T.W. Guo, W.C. Kao, and J.Y. Cheng: J. Laser Micro Nanoeng., 18, (2023) 64.
- [9] J.M. Liu: Opt. Lett., 7, (1982) 196.
- [10] J.Y. Cheng, M.H. Yen, W.C. Hsu, J.H. Jhang, and T.H. Young: J. Micromech. Microeng., 17, (2007) 2316
- [11] M.F. Chen, Y.P. Chen, W.T. Hsiao, and Z.P. Gu: Thin Solid Films, 515, (2007) 8515.
- [12] C. Molpeceres, S. Lauzurica, J.L. Ocaña, J.J. Gandía, L. Urbina, and J. Cárabe: J. Micromech. Microeng., 15, (2005) 1271.
- [13] C. McDonnell, D. Milne, C. Prieto, H. Chan, D. Rostohar, and G.M. O'Connor: Appl. Surf. Sci., 359, (2015) 567.
- [14] M. Park, B.H. Chon, H.S. Kim, S.C. Jeoung, D. Kim, J.I. Lee, H.Y. Chu, and H.R. Kim: Opt. Laser Eng., 44, (2006) 138.
- [15] H. Heffner, M. Soldera, and A.F. Lasagni: Sci. Rep., 13, (2023).
- [16] H.W. Choi, D.F. Farson, J. Bovatsek, A. Arai, and D. Ashkenasi: Appl. Opt., 46, (2007) 5792.
- [17] C. Kerse, H. Kalaycioglu, P. Elahi, B. Çetin, D.K. Kesim, Ö. Akçaalan, S. Yavas, M.D. Asik, B. Öktem, H. Hoogland, R. Holzwarth, and F.O. Ilday: Nature, 537, (2016) 84.
- [18] S.Z. Xiao, E.L. Gurevich, and A. Ostendorf: Appl. Phys A, 107, (2012) 333.
- [19] A. Stratan, A. Zorila, L. Rusen, and G. Nemes: Opt. Eng., 53, (2014).
- [20] H. Mustafa, D.T.A. Matthews, and G.R.B.E. Römer: J. Laser Appl., 32, (2020).
- [21] K. Ellmer: Nat. Photon., 6, (2012) 808.
- [22] W.E. Pickett: J. Supercond., 4, (1991) 397.
- [23] C.H. Park, N. Bonini, T. Sohier, G. Samsonidze, B. Kozinsky, M. Calandra, F. Mauri, and N. Marzari: Nano Lett., 14, (2014) 1113.
- [24] J.M. Ziman: "Electrons and phonons: the theory of transport phenomena in solids", (Clarendon Press; Oxford University Press, Oxford, New York, 2001) p. 270.
- [25] C.T. Lee, Q.X. Yu, B.T. Tang, and H.Y. Lee: Thin Solid Films, 386, (2001) 105.
- [26] J. Calderer: Vacuum, 37, (1987) 441.
- [27] M.M. Hamasha, T. Dhakal, K. Alzoubi, S. Albahri, A. Qasaimeh, S.S. Lu, and C.R. Westgate: J. Dispers. Sci. Technol., 8, (2012) 383.
- [28] T. Tohsophon, A. Dabirian, S. De Wolf, M. Morales-Masis, and C. Ballif: Apl. Mater., 3, (2015).
- [29] D.E. Newbury and N.W. Ritchie: J. Mater. Sci., 50, (2015) 493.
- [30] Y.S. Park, E. Kim, B. Hong, and J. Lee: Mater. Res. Bull., 48, (2013) 5115.

(Received: June 27, 2025, Accepted: November 9, 2025)